

# Forgotten treasures in the HST/FOC UV imaging polarimetric archives of active galactic nuclei

## II. Mrk 463E

T. Barnouin<sup>1\*</sup>, F. Marin<sup>1</sup>, and E. Lopez-Rodriguez<sup>2</sup>

<sup>1</sup> Université de Strasbourg, CNRS, Observatoire astronomique de Strasbourg, UMR 7550, F-67000 Strasbourg, France

<sup>2</sup> Kavli Institute for Particle Astrophysics & Cosmology (KIPAC), Stanford University, Stanford, CA 94305, USA

Received Month Day, 2024; accepted Month Day, 2024

### ABSTRACT

**Context.** The Mrk 463 system is known to host two powerful sources separated by about 4 kpc, both identified as active galactic nuclei (AGN). This makes the Mrk 463 system a unique laboratory to study the geometry and dynamics of galaxy merging and its relation to AGN duty cycles.

**Aims.** The eastern nuclei, Mrk 463E, is the brightest of the two and thus a prime target for a polarimetric study. It is classified as a Seyfert 2 galaxy, meaning that one could expect large polarization degrees from scattering off electrons and dust in the polar winds.

**Methods.** In the continuity of our series of papers, we reduced archived and previously unpublished polarization observations obtained with the Faint Object Camera (FOC) onboard the Hubble Space Telescope (HST), to obtain a high resolution near ultraviolet (near-UV) polarization map of the Mrk 463E nuclei. We coupled this map to near infrared (NIR) and X-ray observations to get a clear picture of the geometric arrangement of matter around the core of Mrk 463E.

**Results.** We found that the nucleus location is further South from the optical peak flux than previously estimated. The strongly polarized conical wind has a half-opening angle of  $\sim 15^\circ$  and display three main periods of mass ejection. Its polarization allowed us to estimate the AGN inclination towards the observer ( $\sim 55^\circ$ ). Finally, our maps revealed a gas streamer connecting Mrk 463E and Mrk 463W, with a tentative detection of a large kpc-scale ordered magnetic field connecting both galaxies.

**Conclusions.** This unpublished observation turned out to offer more than the original proposal asked for and allowed to derive tight geometric and dynamical constraints for Mrk 463E. High resolution radio maps and IR polarimetry are now necessary to further study the jet and the newly discovered gas streamer.

**Key words.** Instrumentation: polarimeters – Methods: observational – polarization – Astronomical data bases: miscellaneous – Galaxies: active – Galaxies: Seyfert

## 1. Introduction

It is now quite accepted that massive galaxies should host a supermassive black hole (SMBH) at their center. The most recent observations from the Event Horizon Telescope provided powerful evidence for their existence in the nearby galaxy M87 (Event Horizon Telescope Collaboration et al. 2019), as well as in the center of our own galaxy (Event Horizon Telescope Collaboration et al. 2022). However their formation and growth remains difficult to trace, even more so if we take into account the parallel evolution of their host galaxy (Di Matteo et al. 2005). Massive black hole mergers and powerful accretion phases, responsible for the so-called Active Galactic Nuclei (AGN), are the main processes thanks to which we explain SMBH growth (Di Matteo et al. 2005; Treister et al. 2012). However, if taken separately, these growth models remain too slow for both galactic and cosmological simulations to explain the observed SMBH masses with respect to their host galaxy age (Capelo et al. 2017; Volonteri et al. 2022). Both processes should occur simultaneously in the lifetime of a black hole to become supermassive. The best place to look for concurrent merging and accretion are probably the Ultra Luminous Infrared Galaxies (ULIRG, Sanders et al. 1988), which are believed to be the ongoing phase or the rem-

nant of a merging process that is able to bring a lot of dust and gas nearby their central SMBH (Barnes & Hernquist 1991; Hopkins et al. 2006). This could trigger an AGN phase and lead to intense SMBH growth at the same time (Treister et al. 2012).

Mrk 463 is a nearby,  $\sim 224$  Mpc (in standard  $\Lambda$ CDM cosmology), merging system consisting of two nuclei, Mrk 463E (east,  $z = 0.05132$ , Lavaux & Hudson 2011) and Mrk 463W (west,  $z = 0.05055$ , Abazajian et al. 2009), separated by  $3.8'' \pm 0.01''$ , which corresponds to a projected distance of  $\sim 4.1$  kpc. Observations in radio (Neff & Ulvestad 1988; Mazzarella et al. 1991), [OIII] and [NII] bands (Hutchings & Neff 1989; Chatzichristou & Vanderriest 1995) were used to study the interconnected nuclei and revealed tidal tails from a recent violent interaction as well as evidences for the ongoing merging of the two galaxies (Hutchings & Neff 1989; Mazzarella et al. 1991). High resolution 6 cm radio observations of the eastern nuclei, Mrk 463E, revealed a small-scale jet ( $0.05''$  to  $1.5''$ ) along a Position Angle (PA) of  $\sim 11^\circ$  (Neff & Ulvestad 1988). At 20 cm, Mazzarella et al. (1991) observed extended but isolated emission sources situated  $18''$  ( $\sim 20$  kpc) south and  $4''$  ( $\sim 5$  kpc) north of Mrk 463E, without optical or IR counterparts. They are not connected to the bright radio emission of the nucleus but, since they are located along the same axis as the small radio jets and have characteristics of classic radio lobes, they were associated to Mrk 463E

\* thibault.barnouin@astro.unistra.fr

as weak radio lobes. The jets associated to Mrk 463E can be extended up to another emission region as far as  $\sim 12$  kpc to the northwest of the nuclei (Neff & Ulvestad 1988; Mazzarella et al. 1991). Such extended radio emission and its strong luminosity density put Mrk 463E in-between the Seyfert and radio-galaxy classification.

Due to its early identification as a type 2 Seyfert galaxy (Shuder & Osterbrock 1981), the eastern nucleus of Mrk 463 has been the focus of polarization studies to determine if the AGN fits the Unified Model (Antonucci 1993). Indeed, Miller & Goodrich (1990) discovered broad emission lines in its polarized spectrum, proving the presence of a type-1 nucleus behind some obscuring material. Broad (full width half-maximum  $\sim 2750$  km·s<sup>-1</sup>) H $\beta$  and H $\alpha$  Balmer lines were detected in polarized flux, with an intrinsic polarization degree of 10% and an electric vector polarization angle of 85° (after correction for interstellar polarization), which was comparable to the other archetypal Seyfert-2 AGN : NGC 1068 (Antonucci & Miller 1985; Tran 1995a,c). Miller & Goodrich (1990) also found a strong 5500 Å continuum linear polarization of 7.7% with a polarization angle of  $\sim 82^\circ$ , almost perpendicular to the radio PA ( $\sim 4^\circ$ , Unger et al. (1986) and Neff & Ulvestad 1988). Similarly to NGC 1068 (Antonucci & Miller 1985), Mrk 463E ionization cones spread along the radio axis and their illumination by the central engine can easily explain such polarization levels and angles. However, the detected narrowing of the [OIII] and [OII] emission lines in the polarized spectrum hinted for unresolved geometric or dynamic features (Miller & Goodrich 1990; Tran 1995c) and sparked new studies of Mrk 463E at higher spatial resolutions.

High resolution imaging of the eastern nucleus in the optical band was obtained with the Planetary Camera (PC) onboard the Hubble Space Telescope (HST) in July 1991. This observation led to the discovery of a sub-arcsec scale jet-like structure around the nucleus (Uomoto et al. 1993). While similar in morphology to the optical jets of M87 and 3C 273, the radio emission in Mrk 463E is positioned just beyond the end of this optical "jet". The optical and radio emission do not correlate and therefore the observed optical emission from this "jet" can not be synchrotron in nature. Because the axis of this polar structure is almost perpendicular to the detected continuum polarization, Uomoto et al. (1993) suggested that it was the scattering site that allows the observation of the hidden Seyfert-1, producing the polarized spectrum observed by Miller & Goodrich (1990). A follow up observation using the Faint Object Camera (FOC) onboard HST was performed in May 1996 to verify this prediction. To this day, those high quality data were never reduced, analyzed nor published, despite some preliminary announcements by Tremonti et al. (1996).

The study of the Mrk 463 system continued at higher energies, especially because the spectral type and true AGN nature of the western nuclei were never confirmed (Shuder & Osterbrock 1981; Neff & Ulvestad 1988). Chandra high-energy (2–8 keV) imaging analysis of the Mrk 463 system revealed the presence of two unresolved X-ray sources, coincident with the two nuclei detected in radio and IR (Bianchi et al. 2008). X-ray spectral analysis using Chandra, XMM-Newton and NuSTAR data showed that Mrk 463W is a Compton-thin obscured AGN ( $n_H \leq 10^{24}$  at/cm<sup>2</sup>) with a small bolometric to X-ray luminosity ratio ( $K_{2-10keV} \sim 1-3$ ), suggesting a low Eddington ratio ( $< 10^{-3}$ ; Yamada et al. 2018). Hence Mrk 463W is most probably in an early phase of AGN activity triggered by the merger event. Regarding the eastern nucleus, the same analysis showed that its intrinsic spectrum is X-ray weak (with respect to its UV luminosity) but is

associated with a high Eddington ratio ( $\lambda_{Edd} = 0.4-0.8$ ; Bianchi et al. 2008; Yamada et al. 2018). This would suggest a Compton-thin obscured AGN with a rapidly growing SMBH. The recent merger event could have triggered efficient gas fueling onto the SMBH without deeply burying the nuclei with gas and dust.

It is thus evident that, thanks to its distance, luminosity and recent history, the Mrk 463 system makes a unique laboratory to study AGN evolution and SMBH growth. A violent interaction between its two nuclei probably triggered their AGN phase, as observed from the radio to the X-rays. Some high resolution archival data still remain to be analyzed to complete and to better understand how the regions interact, what is the nature of the bright, sub-arcsec scale, optical jet-like structure in Mrk 463E and how matter is arranged around this nucleus. Therefore, in this second paper of our series about the archival HST/FOC data, we reduce and analyse for the first time a UV imaging polarimetry observation of the scattering regions of Mrk 463E, requested in 1995, to verify the prediction of Uomoto et al. (1993). In Sect. 2, we present the observation and data reduction techniques. The reduced polarization map is analyzed in details in Sect. 3, making use of the high spatial resolution of the instrument for mapping several specific regions around the nucleus. Sect. 4 puts this observation into a multi-wavelength context to better highlight the different processes at play and understand the nature of the jet-like structure. The results of this analysis are discussed in Sect. 5. Sect. 6 summarizes our findings.

## 2. Observation and Data Reduction

Mrk 463E was observed by the HST/FOC on May 10, 1996 (program ID 5960). This observation was requested as a follow-up of the previous HST/PC observation analyzed and published in Uomoto et al. (1993). Its goal was to inspect in UV light the sub-arcsecond jet-like structure discovered in the optical and determine if it is, indeed, a scattering site. This observation was made in the f/96 mode with the zoom off. It results in pixels of size  $0.014'' \times 0.014''$  for a  $7'' \times 7''$  Field of View (FoV). It used the F342W filter centered around 3404 Å, for a total exposure time of 10,748 seconds, 11,300 seconds and 10,748 seconds through the POL0, POL60 and POL120 filters, respectively. The observation products are stored in different flavors of calibration in the MAST/HST legacy archives of the FOC. The data were retrieved and reduced as described in the first paper of our series (Barnouin et al. 2023). We refer the reader to this paper for an in-depth explanation of the reduction steps and definition of the uncertainties (Section 2.7 in the aforementioned paper,  $\sigma_I$  and  $\sigma_P$ ) used in the following analysis.

For this observation, the FoV of the FOC instrument is centered on the eastern nucleus, putting the western nucleus just outside of the image. A quick analysis reveals small to no contamination of light coming from Mrk 463W: only part of an extended source can be seen in the bottom-right corner of the instrument FoV (as seen in Fig. 1). Thanks to the imaging capacities of the HST/FOC, it is easily filtered out of the eastern nucleus analysis.

The long exposure time through each polarized filter allowed us to obtain statistically significant measurements through our reduction pipeline: in the resampled  $256 \times 256$  pixel resolution of the FOC (Nyquist sampling of the native  $512 \times 512$  pixel image), and without smoothing, we obtain a flux detection (at  $\geq 3\sigma_I$ ) in 33.8% of the pixels, 0.03% of which have a polarization detection ( $\geq 3\sigma_P$ ), amounting to 6 pixels. The retrieved data were not deconvoluted with a Richardson-Lucy algorithm – contrary to what was done in Uomoto et al. (1993) – as we want to study the diffuse emission from the Narrow Line Re-

gion (NLR) and because of the native high signal-to-noise ratio per pixel in the region of interest. In the following section, we thus present an analysis of the polarization map rebinned to pixels of size  $0.05'' \times 0.05''$ , i.e. 3.5 times the native pixel size, and smoothed with a bi-dimensional Gaussian filter with a full-width at half-maximum of  $0.10''$ , i.e. twice the resampled pixel size. Unless specified otherwise, the polarization vectors are shown for a signal-to-noise ratio (S/N) in polarization degree greater than 3:  $[S/N]_P \geq 3$ .

### 3. Polarization Analysis

#### 3.1. The FOC polarization map

Fig. 1 shows the polarization map overlaid on the total intensity image. The polarization vectors are displayed for  $[S/N]_P \geq 3$ , their length is proportional to their polarization degree and they are oriented according to their electric vector polarization angle, from North to East direction, following the IAU convention (IAU 1973). The total flux image is dominated by two hot spots of flux on a North-South axis and whose centers are separated by  $\sim 0.67$  kpc (projected distance). These large hot spots are connected by a narrow flux column, as if an external constraint was creating a physical bottleneck between the two extended flux spots. Intense emission surrounds those two hot spots that forms a well-contrasted, large-scale, cone-shaped region, a geometry already observed for many other Seyfert AGNs (see, e.g. Miller et al. 1991; Wang et al. 2024; Wilson 1996). Such bi-cone (or hourglass-shaped) structure is known to be associated with the NLR, emerging from the (unresolved) vicinity of the black hole and extending hundreds of parsecs along the polar axis of the AGN, often revealed thanks to [O III] mapping (see, e.g. Walker 1968; Oke & Sargent 1968; Mullaney et al. 2013). At the northern extremity of the conical wind, a few ovoid clumps seem to escape the wind towards the North-East direction. The southern part of the Mrk 463E's bi-cone is not visible, likely hidden behind the host galaxy plane (see Sec. 4.1 for further details).

A second, less extended emission originating from the western nucleus, Mrk 463W, can be seen at the South-West border of the FoV. As we lack a good part of the emission from Mrk 463W, we can not infer the geometrical aspect and emission characteristics of the region appearing in this observation. We report no detectable polarization coming from Mrk 463W: the small polarization features seen in Fig. 2 in the western nucleus remain below  $1.5\sigma_P$  and can not be dissociated from noise. However, a stream-like feature extends from the base of the observed polar wind of Mrk 463E in an elliptical arc into the general direction of Mrk 463W. This arc, visible in total flux (see Fig. 1), has no  $[S/N]_P \geq 3$  polarized counterparts (see Fig. 2). See Sect. 5.1 for further details about this arc-like structure.

In the polarized flux map shown in the left-hand part of Fig. 2, we can see that the aforementioned conic wind and ovoid clumps account for almost all of the polarized flux. The cone appears much narrower in polarized flux (half-opening angle of  $\sim 15^\circ$ ) that what can be seen in total flux (half-opening angle of  $\sim 36^\circ$ ), both reported on Fig. 7. This is similar to what has been observed in NGC 1068, for which the ionization cone appears much narrower in polarized flux (Miller et al. 1991). We use both of these cone delimitation to make an estimation of the nucleus location, displayed as a red cross on Fig. 1, 2 and 7. The coordinates of the nucleus, according to our polarization map, are:  $13\text{h}56\text{m}02.91\text{s}$ ,  $18^\circ 22' 16.6''$ .

In polarized flux, a bottleneck-like feature appear between the two hot spots. This apparent bridge between the extended

clumps in the NLR could come from scattering of the UV continuum from the nuclei on material in the parsec-scale radio jet at position angle  $180^\circ$  (Mazzarella et al. 1991; Kukula et al. 1999). This could be investigated by correlating the present near-UV polarization map to high resolution radio maps. Just outside the conical wind,  $\sim 1.5$  kpc East of the southern hot spot, a spherical clump (circled in blue in Fig. 1 and 2) appears in both total and polarized flux with  $P = 19.8 \pm 4.9\%$  at  $\Psi = 76.2 \pm 7.1^\circ$ . Two other spherical clumps (circled in yellow in Fig. 1) are visible in total flux and polarization East of the Northern end of the polar wind, lying at  $\sim 2.8$  kpc and  $\sim 3.5$  kpc East of the major clumps lying North of the NLR cone, with  $P = 37.4 \pm 13.8\%$  at  $\Psi = 148.4 \pm 10.4^\circ$  and  $P = 11.4 \pm 5.9\%$  at  $\Psi = 56.5 \pm 14.8^\circ$  respectively, just below  $2\sigma_P$ . South of the wind, two small knots (circled in green in Fig. 1 and 2) appear in polarization, at  $\sim 0.6$  kpc South-West and  $\sim 1$  kpc South-East of the vertex of the wind cone with  $P = 17.0 \pm 3.3\%$  at  $\Psi = 126.2 \pm 5.5^\circ$  and  $P = 24.4 \pm 4.3\%$  at  $\Psi = 77.0 \pm 5.1^\circ$  respectively.

All those features can be seen on the polarization degree map in the right-hand part of Fig. 2. This map reveals that the polarization inside of the NLR does not exceed 20%, dropping to zero around the center of the bottleneck structure. North of the NLR, the clumps show a polarization degree above 30%, increasing up to almost 50% as they get further away from the first two arcseconds around the supposed position of the SMBH.

The centro-symmetric polarization pattern inside of the polar wind have an orientation that is coherent with the scattering of UV continuum coming from an unresolved source South of the cone. Such centro-symmetric pattern was also observed on IC 5063 and NGC 1068 in the previous paper of this series (Barnouin et al. 2023) and reproduced the results of previous imaging polarimetry of NGC 1068, pin-pointing the location of the nucleus thanks to this circular pattern (Capetti et al. 1995; Kishimoto 1999). We also note that the polarization angle of the escaping clumps North-East of the wind, also hint towards the same unresolved source that is South of the cone. The polarization angle pattern clearly proves the intuition of Uomoto et al. (1993), who suggested that the base of the extended polar wind of Mrk 463E is acting like a mirror, allowing the observation of the hidden broad emission lines in polarized flux.

#### 3.2. Comparison with previous polarimetric analysis

Integrating over the whole HST/FOC FoV yields a total flux of  $F_\lambda^{\text{int}} = (14.41 \pm 0.01) \times 10^{-16}$  ergs  $\text{cm}^{-2} \text{s}^{-1} \text{\AA}^{-1}$ , with a polarization degree  $P^{\text{int}} = 8.8 \pm 0.2\%$  and a global polarization position angle  $\Psi^{\text{int}} = 88.3 \pm 0.5^\circ$ . Cropping the observation to remove Mrk 463W, as it can be seen in Fig. 2 and 3 yields  $F_\lambda^{\text{int}} = (13.05 \pm 0.01) \times 10^{-16}$  ergs  $\text{cm}^{-2} \text{s}^{-1} \text{\AA}^{-1}$ ,  $P^{\text{int}} = 10.1 \pm 0.2\%$  and  $\Psi^{\text{int}} = 88.0 \pm 0.4^\circ$ . This cropped polarization map, only showing Mrk 463E, will be used in the following analysis. Finally, integrating only the contribution from the polar wind (including the escaping clumps) yields a polarization degree  $P^{\text{int}} = 12.5 \pm 0.2\%$  at position angle  $\Psi^{\text{int}} = 87.5 \pm 0.3^\circ$ , clearly indicating that most of the polarized flux comes from reprocessing in the winds. In all cases, the polarization angle is perpendicular to the  $\sim 4^\circ$  radio position angle measured by Unger et al. (1986) and Neff & Ulvestad (1988), as expected for a type-2 AGN.

We can compare our HST/FOC map to previous observations. It is a fairly common target and a plethora of spectropolarimetric data exists. A direct flux-to-flux comparison with Watanabe et al. (2003) validates the flux measured by HST: the authors measured a total flux of  $6.8 \times 10^{-15}$  ergs  $\text{cm}^{-2} \text{s}^{-1} \text{\AA}^{-1}$  at

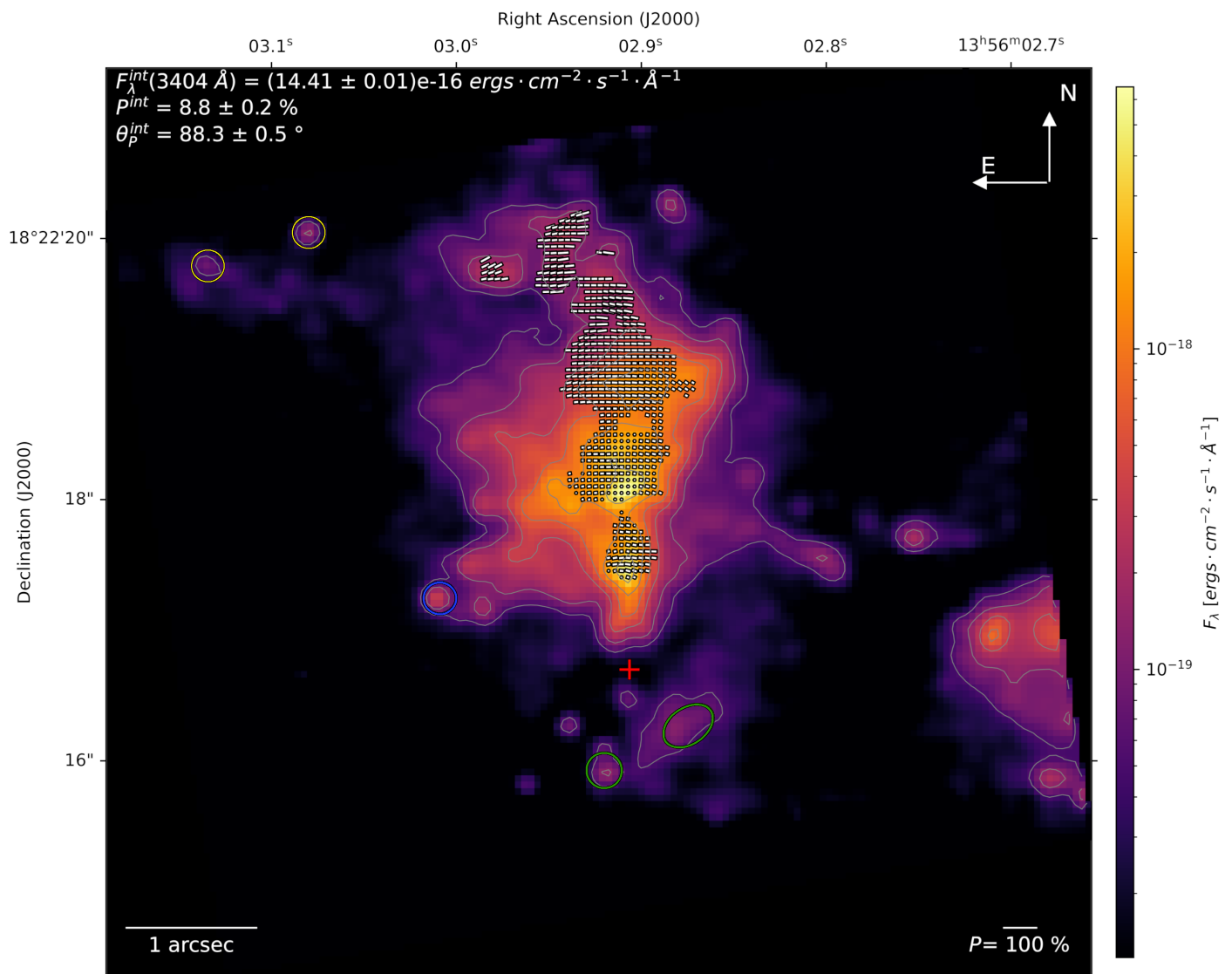


**Fig. 1.** HST/FOC observation of Mrk 463E resampled to pixels of  $0.05'' \times 0.05''$ . Intensity is color-coded in  $\text{erg cm}^{-2} \text{s}^{-1} \text{\AA}^{-1}$ . Polarization vectors are displayed for  $[S/N]_p \geq 3$ . The red cross shows our estimation for the nucleus location. The contours are displayed for 0.8%, 2%, 5%, 10%, 20% and 50% of the maximum flux. Top-left corner values are integrated over the whole FOC FoV ( $7'' \times 7''$ ):  $F_\lambda^{\text{int}} = (14.41 \pm 0.01) \times 10^{-16} \text{ ergs cm}^{-2} \text{ s}^{-1} \text{\AA}^{-1}$  with  $P^{\text{int}} = 8.8 \pm 0.2\%$  and  $\Psi^{\text{int}} = 88.3 \pm 0.5^\circ$ . Circled spots are discussed in sect. 3.1.

5400  $\text{\AA}$  in a  $3''$  extraction window on 2001, February 21. The slight difference between the two fluxes is easily explained due to the different wavelength windows (the total flux spectrum of Mrk 463 rising to the blue) and also to the seeing conditions on Earth ( $1.3 - 1.4''$ ) and (the lack-of) in space. Watanabe et al. (2003) acquired polarized spectra of Mrk 463E from 4600  $\text{\AA}$  to 25000  $\text{\AA}$  and their polarization degree and angle ( $10.4\%$  and  $82^\circ$ ) at 5400  $\text{\AA}$  agree well with our measurements at 3404  $\text{\AA}$ , indicating that electron scattering could be at work here, but the lack of error bars on Watanabe et al. (2003)'s measurements hamper a strong conclusion.

Young et al. (1996) obtained optical and near-IR broad-band polarimetric observations of Mrk 463E using the 3.8m United Kingdom Infrared Telescope (UKIRT) and a  $5.0''$  aperture. They report  $P = 6.48 \pm 0.5\%$  at  $\Psi = 86 \pm 2^\circ$  in the U-band and  $P = 5.78 \pm 0.28\%$  at  $\Psi = 88 \pm 1^\circ$  in the V-band, both in agreement with our full FoV polarization at 3404  $\text{\AA}$  that benefited from less unpolarized light contamination. Mrk 463E was also observed both in imaging polarimetry and spectropolarime-

try with the 3m Shane telescope at Lick observatory. The spectropolarimetric analysis was performed through a North-South oriented,  $2.4''$  wide and  $10''$  long slit (see Fig. 30 in Tran 1995b) and presented in Miller & Goodrich (1990) and Tran (1995a). They obtain a continuum polarization of  $P = 7.6\%$  at  $\Psi = 85^\circ$  in the  $3200 - 7400 \text{\AA}$  (they also report a broad line polarization of  $P = 10\%$  at  $\Psi = 84^\circ$ ). We simulate such slit by integrating the I, Q and U Stokes fluxes inside a  $2.4''$  wide and  $7''$  long slit (limited by the  $7'' \times 7''$  FoV of the HST/FOC) oriented North-South and centered on the [O III] maximum flux, see Fig. 1. We report an integrated flux around 3404  $\text{\AA}$  of  $F_\lambda^{\text{int}} = (12.57 \pm 0.01) \times 10^{-16} \text{ ergs cm}^{-2} \text{ s}^{-1} \text{\AA}^{-1}$  and a polarization degree of  $P = 10.8 \pm 0.2\%$  at position angle  $\Psi = 87.6 \pm 0.4^\circ$ , also compatible with the previously reported optical polarization.

### 3.3. Region specific polarization analysis

The unmatched imaging resolution of the HST/FOC in the near-UV band allows to perform region specific polarimetric stud-

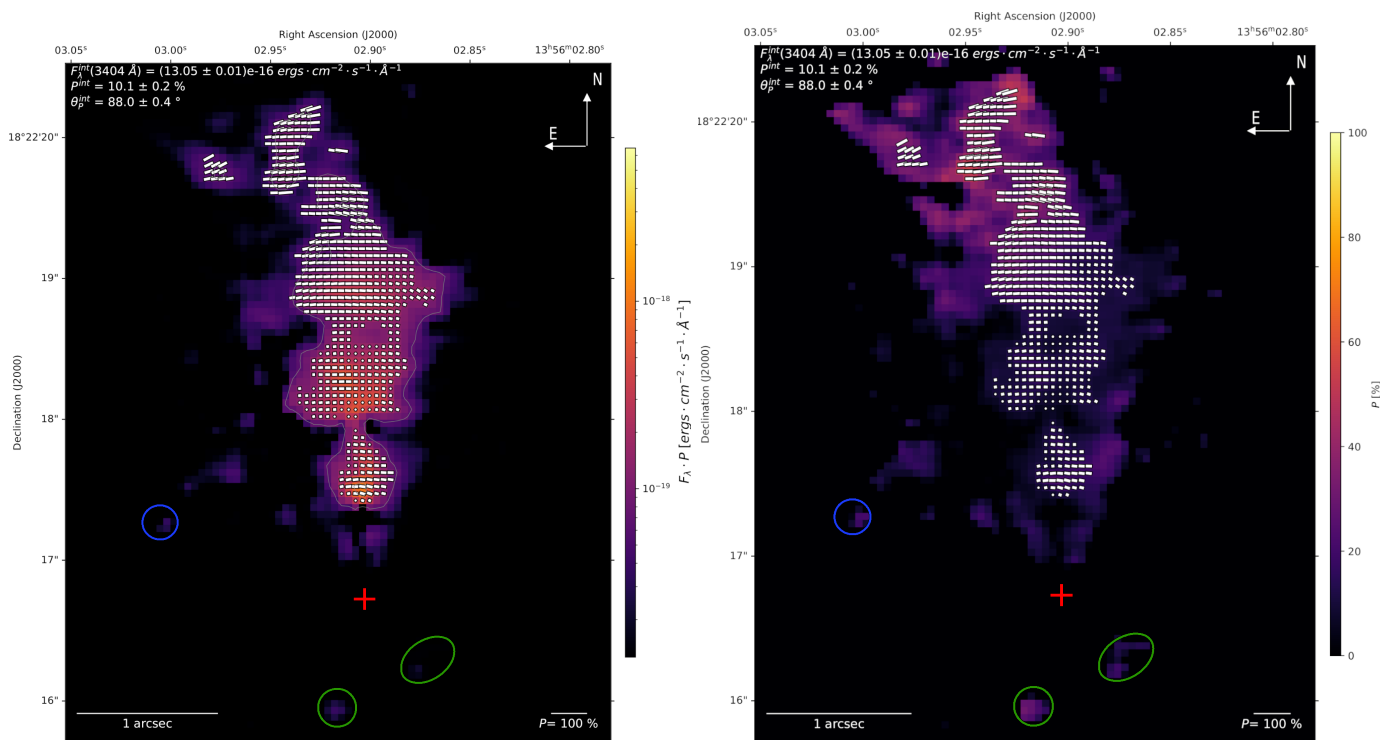


**Fig. 2.** Cropped polarized flux (left) and polarization degree (right) maps highlighting the northern mirror of Mrk 463E. The red cross shows our estimation for the nucleus location. Circled spots are discussed in sect. 3.1.

ies. In the following, we use simulated apertures and slits to obtain integrated polarization characteristics on selected regions. Regions for aperture integration are shown in Fig. 3 on top of the S/N map in polarization degree, with the contribution from Mrk 463W cropped-out. This particular map allow us to select region of high polarization degree, based on the most significant polarization detection. We report the integrated values on each region for flux, polarization degree and angle in Tab. 1.

Regions 1, 2 and 3 correspond to clumpy structures located inside of the northern polar wind showing high polarized fluxes (see Fig. 2). As we probe clumps further away from the nucleus, we move along the polar axis and find that the clumps conserve a polarization angle that is coherent with perpendicular scattering. The slightly different polarization angle  $\Psi^2 \simeq 87.6^\circ$  of region 2 with respect to regions 1 and 3 can easily be explained by the fact that the center of the polarized flux knot is displaced East of the polar axis.

Region 4 was selected to focus on the escaping clumps North-East of the wind. The integrated polarization shows a polarization angle of  $\Psi^4 \simeq 92.5^\circ$ , a few degrees higher than region 1 to 3 in the cone, but still consistent with diffusion of the continuum from the nucleus. These clouds are also characterized by a strong polarization degree of  $P^4 \simeq 34\%$ . This could be due to a variety of reasons, such as less perturbed medium than in the cone, less obscuration along the line-of-sight, higher albedo, etc., which are indistinguishable in this context.

Region 5 corresponds to the location of the hidden southern polar cone. While it is not clear at this stage if the wind is simply absent or obscured (see Sect. 4.1 for further discussion), we wanted to check if polarization could be detected here. We find a small but statistically significant ( $\sim 5.5\sigma_P$ ) polarization degree associated with a polarization angle perpendicular to the jet direction. It indicates that there is a scattering region, likely in the form of a wind (or at least clumps), but the total flux signal seems very attenuated, probably by dust absorption.

Region	Flux ( $10^{-17}$ ergs $\text{cm}^{-2}$ $\text{s}^{-1}$ $\text{\AA}^{-1}$ )	P (%)	PA ( $^\circ$ )
Full FoV	$144.10 \pm 0.10$	$8.8 \pm 0.2$	$88.3 \pm 0.5$
Cropped FoV	$130.50 \pm 0.10$	$10.1 \pm 0.2$	$88.0 \pm 0.4$
Cone+clumps	$105.70 \pm 0.10$	$12.5 \pm 0.2$	$87.5 \pm 0.3$
$2.4'' \times 7''$ slit	$125.70 \pm 0.10$	$10.8 \pm 0.2$	$87.6 \pm 0.4$
1	$14.77 \pm 0.03$	$12.8 \pm 0.4$	$85.3 \pm 0.8$
2	$35.25 \pm 0.05$	$11.0 \pm 0.3$	$87.6 \pm 0.6$
3	$19.16 \pm 0.03$	$17.6 \pm 0.3$	$84.7 \pm 0.5$
4	$3.30 \pm 0.02$	$33.9 \pm 0.9$	$92.5 \pm 0.8$
5	$2.21 \pm 0.02$	$6.0 \pm 1.1$	$99.3 \pm 5.3$
6	$0.96 \pm 0.01$	$3.8 \pm 1.9$	$133.4 \pm 14.3$

**Table 1.** Integrated flux and polarization over several regions of interest (see Fig. 3).

The stream-like feature going from Mrk 463E toward Mrk 463W and visible in total flux only is the focus of region 6. We simulated a  $0.35''$  wide and  $1.15''$  long slit, oriented  $67^\circ$  East of North, to integrate the Stokes fluxes especially along the hypothetical stream. Unfortunately, the detected polarization is below  $3\sigma_P$  and nothing strong can be claimed here without further observation. Nevertheless, if the structure is real, we have hints for a polarization degree  $P^6 = 3.8 \pm 1.9\%$  (with 95% confidence level) at an electric polarization angle  $\Psi^6 = 133.4 \pm 14.3^\circ$ . We will discuss these results in Sect. 5.1.

## 4. Multi-wavelength Analysis

### 4.1. Correlation with HST/WFPC2 near-IR observation

The Mrk 463 system was observed using the Wide Field Planetary Camera 2 (WFPC2) onboard HST in November 1995 as part of a sample of ten near infrared quasars (Proposal ID 5982). The binary system was observed through the F814W filter, centered around  $7996 \text{ \AA}$  with a bandwidth of  $646 \text{ \AA}$ . The results of this observation were published in Sanders & Mirabel (1996). While

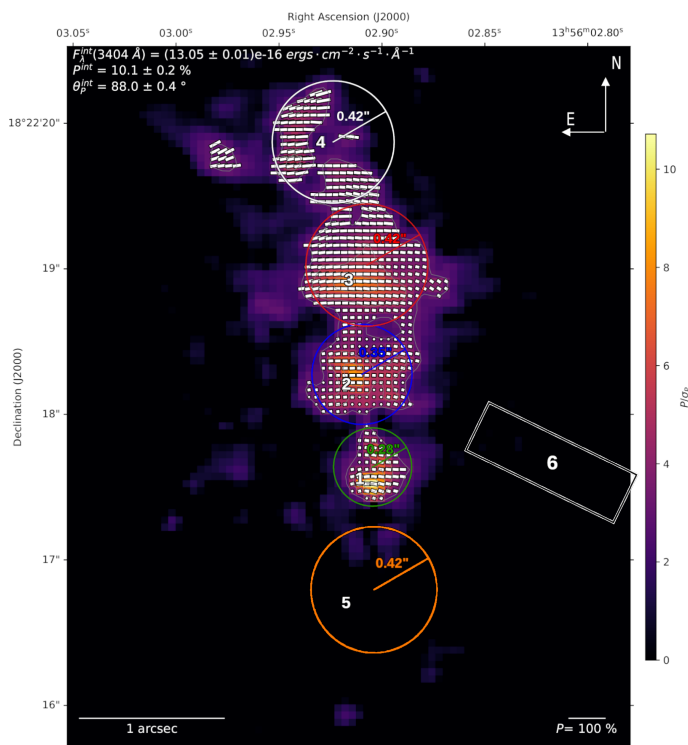


**Fig. 3.** Knots in the North polar wind. The 6<sup>th</sup> region corresponds to a simulated slit aperture of  $0.35'' \times 1.15''$  along the stream-like feature that can be observed in Fig. 1 and which is discussed in Sect. 5.1.

the WFPC2 has a spatial resolution similar to the FOC (pixels of size  $0.0455'' \times 0.0455''$ ), it benefits from a much wider FoV of  $36'' \times 36''$ . We thus decided to take advantage of the WFPC2 observation of Mrk 463E in order to better understand the geometric configuration of matter around the nucleus, as well as its composition.

We downloaded and reduced the WFPC2 data, and overlaid in Fig. 4 the FOC total intensity (gray contours) and polarization (white vectors) maps on top of the near-infrared total intensity map taken with the F814W filter. Both maps were aligned on similar-looking punctual and extended features, as it can be seen on the zoomed box in the right-hand part of Fig. 4. The wider FoV of WFPC2 allowed to observe both nuclei at once and better assessed the contribution of the western object to the FOC image. From this simple overlay we can see that the Mrk 463E maximum intensity regions in near-UV and near-IR do not overlap, with the IR peak being just south of the UV peak. We also note that the stream-like feature seen West of Mrk 463E and extending in the general direction of Mrk 463W in the UV intensity map also appear in the IR intensity map, reinforcing the probability of being a real structure and not an observational artifact of the FOC.

Because the near-UV and near-IR maps have the same pixel size and have been properly aligned, it is possible to subtract one from the other. This is what we did to obtain the excess UV map, visible in Fig. 5. It is a worthwhile exercise as the UV excess can be used to determine whether the UV light could be attributed to recent star formation (which, in turn, can be linked to evolutionary processes in the host galaxy) or a direct consequence of the AGN activity (Fabian 1989). Our map clearly shows that the latter explanation is correct in the case of Mrk 463E: the UV excess perfectly matches the polar wind geometry. It is thus a solid evidence advocating for reprocessing of the thermal emission from

the nucleus onto the Northern winds. Additionally, it indicates that the Northern winds are located in front of the host's galactic plane, in a similar fashion than NGC 1068 (Kishimoto 1999). The Southern winds are very likely obscured by the dusty content of the host galaxy. It is interesting to note that there is a deficit of UV photons precisely at the base of the northern wind. Correlating this UV-excess map to radio maps of the parsec-scale jets could provide additional information to constrain more precisely the location of the nucleus.

#### 4.2. Correlation with Chandra 2-8 keV observation

In the high energy domain, where photon fluxes are weaker, it is not easy to acquire high resolution images. It is detrimental because arcsecond X-ray imaging could provide a wealth of information about black hole growth with time, through mergers (likewise like Mrk 463E) or AGN fueling (Mushotzky et al. 2019). Luckily, the Chandra X-ray Observatory was pointed toward this system in June 2004 (ObsId 4913) at took full advantage of its Advanced CCD Imaging Spectrometer (ACIS). The observation allowed for the first, firm identification of both nuclei as Seyfert-2s (Bianchi et al. 2008).

Similarly to the WFPC2 case, we downloaded and reduced the data in order to overlay the soft X-ray emission onto the FOC map. The result of such exercise is presented in Fig. 6. The alignment was more complex as the spatial resolution of the Chandra map ( $0.492'' \times 0.492''$ ) is one order of magnitude "worse" than that of the HST/FOC. We used the fact that both AGNs (Mrk 463E and Mrk 463W) were observed by Chandra to align the two objects with the near-UV map. Ultimately, we can see that the peak of X-ray emission is consistent with the peak of near-UV flux in the first arcsecond around the hidden nucleus, but subtle details are elusive. We also see that, despite the X-rays being more extended than the UV emission, the two nuclei are well separated on the Chandra map, confirming the non-contamination of the Mrk 463E HST/FOC image from the western nucleus.

## 5. Discussion

### 5.1. A gas streamer connecting Mrk 463E and Mrk 463W?

Thanks to the sharp contrast of the total flux of the HST/FOC UV map against the diffuse background, we observed an elongated faint source extending from the northern wind of Mrk 463E towards the South-West, in the general direction of Mrk 463W (see Fig. 1). This stream has an IR counterpart in the WFPC2 observation, slightly less contrasted than in the FOC map. This IR/UV comparison allows us to confirm that the stream has a pronounced curvature that connects to the base of the northern wind of Mrk 463E (see Fig. 4). For this reason, one might think that it is a stream of gas and dust linked to the past encounter between Mrk 463E and Mrk 463W, rather than a filament related to the AGN winds.

In order to analyze this structure more closely, we integrated the polarization of such stream on the HST/FOC image using a simulated slit of  $0.35'' \times 1.15''$  at a  $67^{\circ}$  angle, so that it gets a maximum of flux from the stream itself and as little pollution as possible from the AGN wind and the background. The polarization, reported in Sect. 3.3 and Tab. 1, hints for an electric vector polarization angle of  $\Psi^6 \sim 133^{\circ}$ . Such polarization angle is inconsistent with the hypothesis that the AGN nuclei (either Mrk 463E or Mrk 463W) are the primary sources of radiation scattering onto the stream. For example, for a scattering target

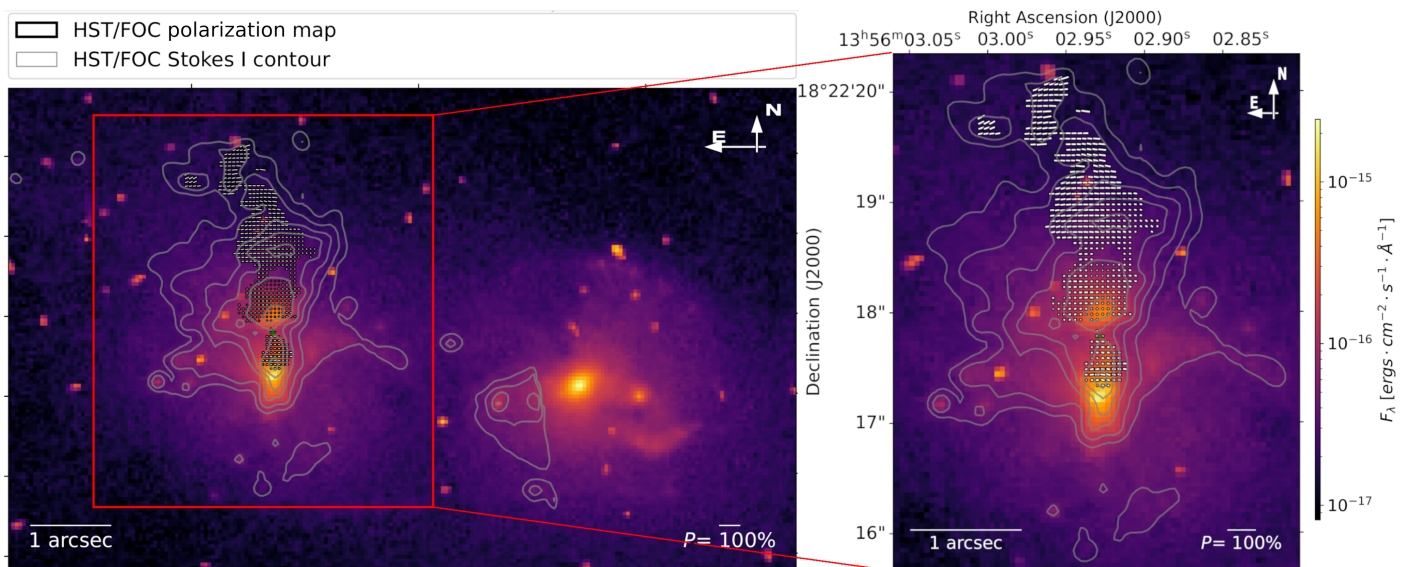


**Fig. 4.** WFPC2 observation of Mrk 463, overlaid with the polarization vectors obtained from the FOC observation analysis. Both near-IR and near-UV maps were aligned on similar looking features around the nucleus of Mrk 463E.

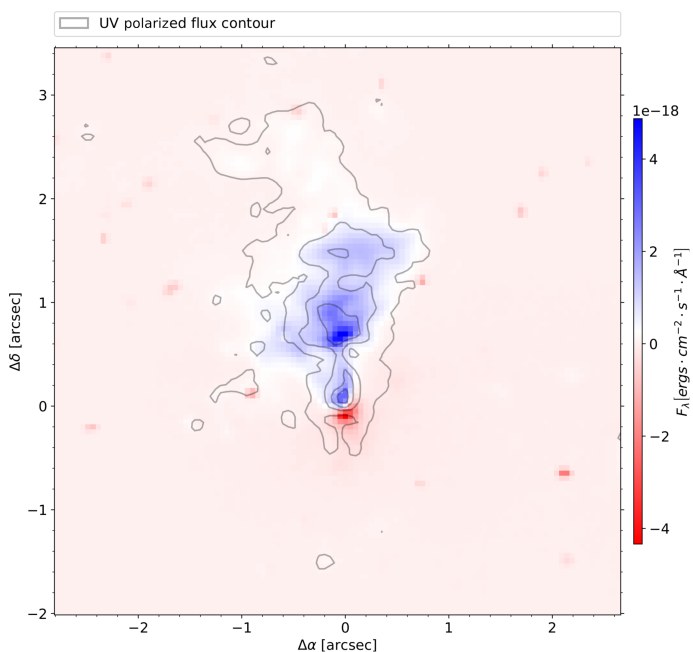


**Fig. 5.** HST/WFPC2 image at 7996 Å subtracted to the HST/FOC image at 3404 Å. Both maps were binned to 0.05'' pixel size and aligned on similar looking features. The contours display the level of near-UV polarized flux, correlated with the polar wind of the AGN.

located at the center of our extraction region, the line orthogonal to the direction towards the hidden nucleus of Mrk 463E would correspond to a polarization angle of 41°.

The polarization from this potential stream is thus uncorrelated to the AGN (otherwise, it would have probably appeared on the UV excess map too). The fact that the magnetic vector, orthogonal to the measured electric vector polarization angle, roughly aligns with the stream direction suggests that the origin of the polarization could very well be dichroic absorption from Mrk 463E host starlight (or within the stream itself) in the foreground dusty stream (we recall that Mrk 463E is situated further away than Mrk 463W from us). The integrated polarization angle

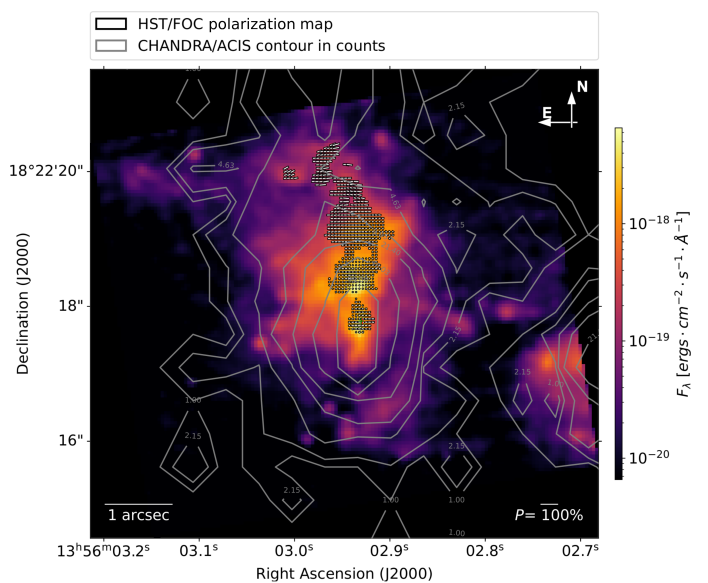


**Fig. 6.** Chandra observation of Mrk 463E, shown with contours overlaid on the FOC observation analysis. The contours corresponds to every tenth percentile of the maximum Chandra flux.

could then highlight the large kpc-scale ordered magnetic field in the stream. Indeed, such gas streamers with highly compressed magnetic fields have been found in interacting galaxies both in radio (Drzazga et al. 2011) and far-IR (Lopez-Rodriguez et al. 2023). Despite a measurement at 95% confidence level only, the number of evidences pointing toward a real stream connecting both nuclei are intriguing. New IR and radio observations are mandatory to explore this feature in more depth.

## 5.2. What do the winds tell us?

The polarization map allows us to study the two components of the polar winds – the NLR and the ionization cone, the former being visible in total intensity and the later in polarized flux. Both are well geometrically delimited against the background emission, so we can measure their half opening angle in Fig. 7.

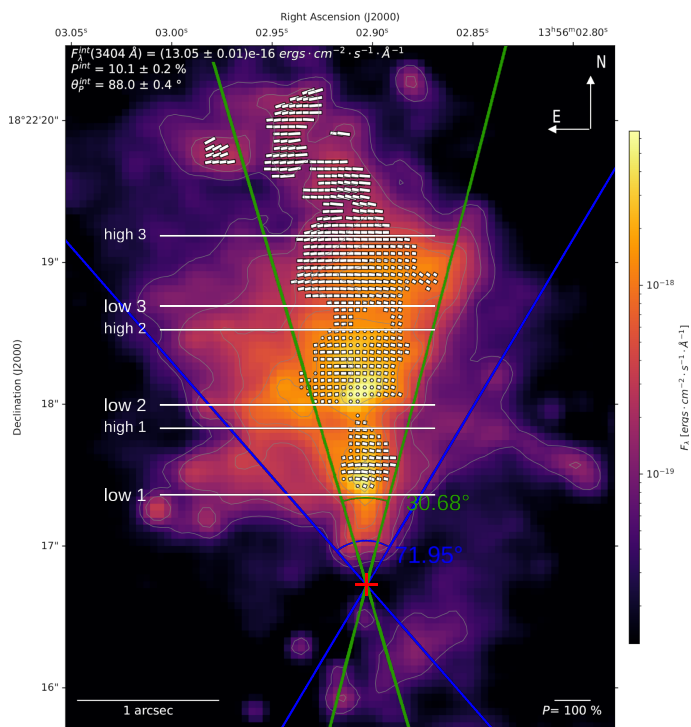


**Fig. 7.** Total intensity near-UV map from the HST/FOC cropped around Mrk 463E northern winds. The blue and green lines represent the total opening angle for the wind cones as seen in total flux ( $71.95^\circ$ ) and polarized flux ( $30.68^\circ$ ), respectively. The red cross shows our estimation for the nucleus location.

The NLR shows an half opening angle of  $\sim 36^\circ$  with respect to the jet axis of the system, which is in agreement with the first results from Tremonti et al. (1996), while the ionization cone, revealed in polarized flux, only has a half opening angle of  $\sim 15^\circ$ . Inside the ionized cone, the polarization angle stays uniform at  $\sim 90^\circ$  with very small dispersion. On average, high polarization degrees are well correlated with peaks of total flux intensity, which can be related to higher cloud densities. We report almost no polarization around the bottleneck between the two UV hot spots (the region between the white lines noted "high 1" and "low 2" on Fig. 7). This could result from kinematics constraints inside the wind, sudden lack of scatter material in this region or from a variation in the past ejection activity of Mrk 463E. In the latter case, continuum photons may scatter on the radio jet between two periods of mass ejection, which would explain the bridge-like feature in both total flux and polarized flux. High resolution imaging of the radio jets is required to confirm this hypothesis.

From the excess map in Fig. 5, we now know that the northern wind is above the host galaxy's plan, a result that is confirmed by the observation of negative velocity with respect to the systemic velocity obtained from mapping the [OIII] 5007 Å line emission, see Fig. 12 (left) in Treister et al. (2018). However, the inclination of the winds is unknown. We may still try to infer the global inclination of the AGN thanks to polarimetry. If we assume that the UV radiation we measured consists of only radiation scattered by free electrons and no other diluting component exists, we can then deduce the scattering angle from the nuclei towards the line of sight within the framework of single scattering:

$$P = \frac{1 - \mu^2}{1 + \mu^2}, \quad (1)$$

Region	Angular size (arcsec)	Propagation time (Myr)
lower 1	0.64	3.21
higher 1	1.08	5.43
lower 2	1.27	6.38
higher 2	1.75	8.84
lower 3	2.00	10.08
higher 3	2.44	12.30

**Table 2.** Angular distance from the nucleus to the inner and outer edges of each cloud and its corresponding propagation time, computed from Eq.2. Each distance is taken from the apex of the cone to the associated region indicated in Fig.7.

where  $\mu = \cos \theta$  and  $\theta$  is the scattering angle. This relation works well if the scattering target size is small enough compared with the distance to the illuminating source (Kishimoto 1999). Considering only pixels with  $[S/N]_p \geq 5$  in region 3 (see Fig. 3), we find an averaged  $P$  of  $20.8 \pm 0.6\%$ , which translates into two solutions for  $\theta$ :  $\theta_1 = 144.1 \pm 0.5^\circ$  and  $\theta_2 = 35.9 \pm 0.5^\circ$  (uncertainties on  $\theta$  were propagated from the previous formula). As a result, we can conclude that Mrk 463E is probably inclined by about  $90^\circ - 35.9^\circ = 54.1^\circ$  (rounded to a value of  $55^\circ$  for simplicity) with respect to the jet axis, well within the expected range of inclinations for a type-2 object (Marin 2014, 2016).

Additionally, the shape of the winds, revealed both in total flux and polarimetry, shows three regions (regions 1, 2 and 3 in Fig. 3) which resemble compact clusters of material illuminated by the hidden nuclei and separated by regions of flux under-density. This could correspond to periods of massive polar ejection spaced by periods of calmer nuclear activity. Those gaps between the different clumps of matter are particularly visible in the polarized flux map between region 1 and 2 (see Fig. 2). Now that we have a tentative value for the inclination of the AGN, we can estimate the duration of the activity periods that lead to massive polar ejection. Based on our analysis, we suppose an inclination angle towards the observer of  $\theta_{\text{incl}} = 55^\circ$  and a uniform wind velocity  $V = 350 \text{ km s}^{-1}$  (Treister et al. 2018). Given the hypothesis that the origin of the wind is the nucleus (Joh et al. 2021), whose location is determined by the cone apexes in Fig. 7, we can deduce the propagation time:

$$T = \frac{a_z \cdot A^{\text{obs}}}{V \cdot \cos \theta_{\text{incl}}} \simeq 5.0455 \cdot A^{\text{obs}} \text{ Myr}, \quad (2)$$

where  $a_z$  is the angular to linear size conversion factor for Mrk 463E at  $z = 0.05132$  in standard  $\Lambda$ CDM cosmology, and  $A^{\text{obs}}$  is the observed angular size on the HST/FOC map in arcsec. We report the results in Tab. 2. From our analysis, we deduce that the clouds comprised in regions 1, 2 and 3 in Fig. 3 were ejected from the nuclei about 4.3, 7.6 and 11.2 Myr ago respectively. These three clouds display similar ejection duty cycles, with massive ejection lasting for 2.3 Myr, with 1.1 Myr of quiet state in-between. Such orders of magnitude are representative of typical AGN duty cycles such as estimated by, e.g., Turner (2018), Biava et al. (2021) or Maccagni et al. (2021).

## 6. Conclusion

In this second paper of our series, we made use of the general pipeline for reduction of the HST/FOC archival data presented in Barnouin et al. (2023) to perform the analysis of a previously unpublished dataset. The archived observation of Mrk 463E revealed to be a true forgotten treasure and a great



illustration of the strength of high spatial resolution UV polarimetry. The strong polarized flux from the source made it possible to extensively study the NLR and granted us an improved estimation of the location of the nucleus, further South than what was previously suggested (estimated coordinates: 13h56m02.91s, 18°22'16.6").

This high angular resolution polarization map also gave a tight estimation of the AGN inclination angle, which we found to be about 55°. We also measured the polar wind's half opening angle between 15° (in polarization) and 35° (in total flux). The observed polarization is in good agreement with previous spectropolarimetric studies of Mrk 463E and calls for additional IR studies of the stream-like feature (the gas streamer) between the two interacting nuclei of the system. This analysis can further be completed with high resolution radio imaging of the jets to better understand their interaction with the observed NLR.

*Acknowledgements.* TB and FM would like to acknowledge the support of the CNRS, the University of Strasbourg, the PNHE and PNCG. This work was supported by the "Programme National des Hautes Énergies" (PNHE) and the "Programme National de Cosmologie et Galaxies (PNCG)" of CNRS/INSU co-funded by CNRS/IN2P3, CNRS/INP, CEA and CNES. E.L.-R. is supported by the NASA/DLR Stratospheric Observatory for Infrared Astronomy (SOFIA) under the 08\_0012 Program. SOFIA is jointly operated by the Universities Space Research Association, Inc. (USRA), under NASA contract NNA17BF53C, and the Deutsches SOFIA Institut (DSI) under DLR contract 500K0901 to the University of Stuttgart. E.L.-R. is supported by the NASA Astrophysics Decadal Survey Precursor Science (ADSPS) Program (NNH22ZDA001N-ADSPS) with ID 22-ADSPS22-0009 and agreement number 80NSSC23K1585.

## References

- Abazajian, K. N., Adelman-McCarthy, J. K., Agüeros, M. A., et al. 2009, *ApJS*, 182, 543
- Antonucci, R. 1993, *ARA&A*, 31, 473
- Antonucci, R. R. J. & Miller, J. S. 1985, *ApJ*, 297, 621
- Barnes, J. E. & Hernquist, L. E. 1991, *ApJ*, 370, L65
- Barnouin, T., Marin, F., Lopez-Rodriguez, E., Huber, L., & Kishimoto, M. 2023, *A&A*, 678, A143
- Bianchi, S., Chiaberge, M., Piconcelli, E., Guainazzi, M., & Matt, G. 2008, *MNRAS*, 386, 105
- Biava, N., Brienza, M., Bonafede, A., et al. 2021, *A&A*, 650, A170
- Capelo, P. R., Dotti, M., Volonteri, M., et al. 2017, *MNRAS*, 469, 4437
- Capetti, A., Macchetto, F., Axon, D. J., Sparks, W. B., & Boksenberg, A. 1995, *ApJ*, 452, L87
- Chatzichristou, E. T. & Vanderriest, C. 1995, *A&A*, 298, 343
- Di Matteo, T., Springel, V., & Hernquist, L. 2005, *Nature*, 433, 604
- Drzazga, R. T., Chyży, K. T., Jurusik, W., & Wiórkiewicz, K. 2011, *A&A*, 533, A22
- Event Horizon Telescope Collaboration, Akiyama, K., Alberdi, A., et al. 2022, *ApJ*, 930, L12
- Event Horizon Telescope Collaboration, Akiyama, K., Alberdi, A., et al. 2019, *ApJ*, 875, L1
- Fabian, A. C. 1989, *MNRAS*, 238, 41P
- Hopkins, P. F., Hernquist, L., Cox, T. J., et al. 2006, *ApJS*, 163, 1
- Hutchings, J. B. & Neff, S. G. 1989, *AJ*, 97, 1306
- IAU. 1973, *Transactions of the International Astronomical Union*, 15, 165–167
- Joh, K., Nagao, T., Wada, K., Terao, K., & Yamashita, T. 2021, *PASJ*, 73, 1152
- Kishimoto, M. 1999, *ApJ*, 518, 676
- Kukula, M. J., Ghosh, T., Pedlar, A., & Schilizzi, R. T. 1999, *ApJ*, 518, 117
- Lavaux, G. & Hudson, M. J. 2011, *MNRAS*, 416, 2840
- Lopez-Rodriguez, E., Borlaff, A. S., Beck, R., et al. 2023, *ApJ*, 942, L13
- Maccagni, F. M., Serra, P., Gaspari, M., et al. 2021, *A&A*, 656, A45
- Marin, F. 2014, *MNRAS*, 441, 551
- Marin, F. 2016, *MNRAS*, 460, 3679
- Mazzarella, J. M., Gaume, R. A., Soifer, B. T., et al. 1991, *AJ*, 102, 1241
- Miller, J. S. & Goodrich, R. W. 1990, *ApJ*, 355, 456
- Miller, J. S., Goodrich, R. W., & Mathews, W. G. 1991, *ApJ*, 378, 47
- Mullaney, J. R., Alexander, D. M., Fine, S., et al. 2013, *MNRAS*, 433, 622
- Mushotzky, R., Aird, J., Barger, A. J., et al. 2019, in *Bulletin of the American Astronomical Society*, Vol. 51, 107
- Neff, S. G. & Ulvestad, J. S. 1988, *AJ*, 96, 841
- Oke, J. B. & Sargent, W. L. W. 1968, *ApJ*, 151, 807
- Sanders, D. B. & Mirabel, I. F. 1996, *ARA&A*, 34, 749
- Sanders, D. B., Soifer, B. T., Elias, J. H., et al. 1988, *ApJ*, 325, 74
- Shuder, J. M. & Osterbrock, D. E. 1981, *ApJ*, 250, 55
- Tran, H. D. 1995a, *ApJ*, 440, 565
- Tran, H. D. 1995b, *ApJ*, 440, 578
- Tran, H. D. 1995c, *ApJ*, 440, 597
- Treister, E., Privon, G. C., Sartori, L. F., et al. 2018, *ApJ*, 854, 83
- Treister, E., Schawinski, K., Urry, C. M., & Simmons, B. D. 2012, *ApJ*, 758, L39
- Tremonti, C. A., Uomoto, A., Antonucci, R. R. J., et al. 1996, in *Bulletin of the American Astronomical Society*, Vol. 28, 1287
- Turner, R. J. 2018, *MNRAS*, 476, 2522
- Unger, S. W., Pedlar, A., Booler, R. V., & Harrison, B. A. 1986, *MNRAS*, 219, 387
- Uomoto, A., Caganoff, S., Ford, H. C., et al. 1993, *AJ*, 105, 1308
- Volonteri, M., Pfister, H., Beckmann, R., et al. 2022, *MNRAS*, 514, 640
- Walker, M. F. 1968, *AJ*, 73, 854
- Wang, C., Wang, J., Dadina, M., et al. 2024, *ApJ*, 962, 188
- Watanabe, M., Nagata, T., Sato, S., Nakaya, H., & Hough, J. H. 2003, *ApJ*, 591, 714
- Wilson, A. S. 1996, *Vistas in Astronomy*, 40, 63
- Yamada, S., Ueda, Y., Oda, S., et al. 2018, *ApJ*, 858, 106
- Young, S., Hough, J. H., Efstathiou, A., et al. 1996, *MNRAS*, 281, 1206